UV-photoexcitation and ultrafast dynamics of HCFC-132b (CF 2 ClCH 2 Cl)

Gessenildo Pereira Rodrigues, Elizete Ventura, Silmar Andrade Do Monte, Mario Barbatti

UV-Photoexcitation and Ultrafast Dynamics of HCFC-132b (CF_2ClCH_2Cl)

Gessenildo Pereira Rodrigues[1,2*], Elizete Ventura[1], Silmar Andrade do Monte[1], Mario Barbatti[2,3*]

[1]*Universidade Federal da Paraiba,*
58059-900, Joao Pessoa-PB, Brazil.
[2]*Max-Planck-Institut für Kohlenforschung,*
Kaiser-Wilhelm-Platz 1, 45470 Mülheim an der Ruhr, Germany.
[3] *Aix Marseille Université, CNRS, ICR UMR7273, 13397 Marseille, France.*
[*] *E-Mail adresses:gessenildo@quimica.ufpb.br (GPR); mario.barbatti@univ-amu.fr (MB)*

Abstract

The UV-induced photochemistry of HCFC-132b (CF_2ClCH_2Cl) was investigated by computing excited-state properties with time-dependent density functional theory (TDDFT), multiconfigurational second-order perturbation theory (CASPT2), and coupled cluster with singles, doubles and perturbative triples (CCSD(T)). Excited states calculated with TDDFT show good agreement with CASPT2 and CCSD(T) results, correctly predicting the main excited-states properties. Simulations of ultrafast nonadiabatic dynamics in the gas phase were performed, taking into account 25 electronic states at TDDFT level starting in two different spectral windows (8.5±0.25 and 10.0±0.25 eV). Experimental data measured at 123.6 nm (10 eV) is in very good agreement with our simulations. The excited-state lifetimes are 106 and 191 fs for the 8.5 and 10.0 eV spectral windows, respectively. Internal conversion to the ground state occurred through several different reaction pathways with different products, where 2Cl, C-Cl bond breakage, and HCl are the main photochemical pathways in the low-excitation region, representing 95% of all processes. On the other hand, HCl, HF, and C-Cl bond breakage are the main reaction pathways in the higher excitation region, with 77% of the total yield.

Introduction

Hydrochlorofluorcarbons (HCFCs) were adopted as direct substitutes of chlorofluorocarbons (CFCs), as the use of these compounds was prohibited by the Montreal Protocol.[1] CFCs have ozone deflection properties, promoted by chlorine atoms in a catalytic process of chain reactions.[2] Usage of HCFCs was justified by their ability to react with OH radicals in the lower atmosphere; hence, fewer molecules interfere in the natural ozone cycle in the upper atmosphere. However, HCFCs show strong thermal absorption of infrared radiation in the region of the atmospheric window and clearly contribute to global warming. The same holds for their substitutes, hydrofluorocarbons (HFCs).[3,4,5] Consequently, the HCFCs were targeted to have their production gradually reduced until 2020.[1,6-8]

The 1,2-Dichloro-1,1-Difluoroethane (CF_2ClCH_2Cl), industrially known as Freon-132b or HCFC-132b (see Fig 1), was the major compound used for replacing CFC-113 (CF_2Cl-$CFCl_2$) in different industrial applications.[9-11] However, its availability is limited due to its toxicity level[12] and effects on metabolism.[13,14] A number of studies involving the HCFC-132b properties have already been performed,[15,16,17] although studies about the photochemical process are scarce.

In terms of photochemistry, one interesting feature of this group of compounds is that a number of competitive reaction channels are possible. Products as hydrogen chloride, hydrogen fluoride, Cl_2 (or 2Cl) elimination, C-Cl and C-C bond rupture have already been observed in different halo-substituted ethanes.[18-20] In the case of gaseous CF_2ClCH_2Cl, Yano *et al.*[21] have studied its infrared multiphoton decomposition. They have detected CF_2CHCl as the dominant product and smaller but still significant amounts of CF_2CH_2, CFClCHCl, and CHCF. The authors have concluded that the primary multiphoton photodecomposition processes involve molecular elimination of HCl and HF and, to a much minor extent, C-C bond rupture. Primary photochemical processes for the HCFC-132b molecule were studied at 147 nm by Yano and Tschulkow-Roux.[22] These authors have reported the importance of chlorine atoms in the main photochemical deactivation, where the most probable dissociation pathway is the elimination of excited Cl_2 molecule or 2Cl radicals; HCl elimination is also observed.

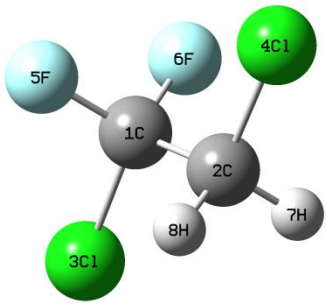

Figure 1. Molecular structure of HCFC-132b with the atomic labels used in this work.

Recently, we have characterized the photolysis process of $C_2F_3H_2Cl$ (HCFC-133a) through excited-state calculations and nonadiabatic dynamics simulations.[23,24] To further investigate how the increasing number of Cl atoms alter the photochemistry of chloroethanes, in the present work we focus on the photochemistry of HCFC-132b (CF_2ClCH_2Cl) in the range up to ~10.7 eV, using multiconfigurational second-order perturbation theory (CASPT2) and time-dependent density functional theory (TDDFT). The UV photoabsortion spectrum has also been simulated and the ultrafast dynamics have been performed at TDDFT level in two different spectral windows, with the aim of characterizing the photochemical deactivation pathways of the CF_2ClCH_2Cl, as well as the influence of the excitation window on its photo-decay processes.

Computational Details

In the first part of the computational studies, the ground-state geometry of the HCFC-132b was optimized and characterized by frequency calculation at the second-order Møller-Plesset (MP2)[25] level with the aug-cc-pVTZ basis set[26] using GAUSSIAN 09.[27] Cartesian coordinates of the minimum geometry is given in the Supporting Information S3. At this minimum, excited-state calculations were performed using the complete active space with second-order perturbation theory (CASPT2), the equation-of-motion coupled cluster method restricted to single, double, and perturbative correction for connected triple excitations (EOM-CCSD(T)), and the time-dependent density functional theory (TD-DFT). The aug-cc-pVDZ (for C, F and H atoms) and d-aug-cc-pVDZ (for Cl atom) basis sets[28,29] were used in the present calculations, where the latter was used for a correct description of Rydberg orbitals. CASPT2 calculations were performed using MOLCAS

program,[30] EOM-CCSD(T) calculations were executed with GAMESS code[31], while the TDDFT calculations were carried out with CAM-B3LYP[32], ωB97XD[33] and M06-2X[34] functionals using GAUSSIAN 09. Twenty four singlet excited states were computed without symmetry restrictions. The C_s symmetry was considered for orbitals classification, with the symmetry plane corresponding to the yz plane and the z axis lying along the $R_{C(2)\text{-}Cl(4)}$ bond. The CASPT2 calculations were performed with a level shift of 0.2 a.u. and a default IPEA shift of 0.25 a.u. The multi-state (MS) method, which couples the twenty-five electronic states included in the calculations, was employed. The active space consists of 12 electrons and 12 orbitals [CAS(12,12)]. At the ground-state geometry they comprise six occupied orbitals: the sigma bonding orbitals of $C_{(1)}$-$Cl_{(3)}$ ($\sigma_{C(1)Cl(3)}$) and $C_{(2)}$-$Cl_{(4)}$ ($\sigma_{C(1)Cl(4)}$) bonds, the following four Cl lone pairs orbitals ($n_{xCl(3)}$, $n_{yCl(3)}$, $n_{xCl(4)}$ and $n_{yCl(4)}$), and six unoccupied orbitals ($\sigma^*_{C(1)Cl(3)}$, $4p_y$, $4p_x$, $\sigma^*_{C(2)Cl(4)}$, 4s and $4p_z$). Graphical representation of the molecular orbitals composing the complete active space is given at the Supporting Information (Figure S1).

Relaxed potential-energy-curve calculations along the $R_{C\text{-}Cl}$ coordinates have been computed on ground-state relaxed geometries for the ground and twenty four excited states. The calculations have been carried out at the CASPT2 level. The distances considered for both CCl bonds varied approximately from 1.83 to 3.83 Å with steps of 0.1 Å. Equivalent curves were also computed at the TD-DFT level with the ωB97XD functional, to check its reliability for the nonadiabatics dynamics simulations.

In the second part of the computational studies, UV photoabsortion spectrum and nonadiabatic dynamics simulations were carried out to understand the ultrafast decay of the excited states of HCFC-132b in the gas phase. Dynamics simulations were performed with the surface hopping method[35,36] based on the fewest switches algorith[35] with decoherence corrections (α = 0.1 a.u.).[37] Quantum equations were integrated with 0.025 fs, while classical integration was done with a time step of 0.5 fs. Interpolation between classical steps was done to obtain all quantities necessary for quantum integration. These calculations have been performed at the TDDFT level (with the ωB97XD functional) using NEWTON-X[38,39] interfaced with GAUSSIAN 09. Nonadiabatic coupling terms were explicitly computed only between excited states, as linear-response TD-DFT in the adiabatic approximation[40] does not properly describe these terms as one of the states is the ground state.[41] For this reason, trajectories ran for a maximum of 1000 fs or until they

reached an S_1/S_0 energy gap smaller than 0.1 eV. The time elapsed to reach this threshold was taken as an estimate of the transition time between the first excited and the ground state. After reaching the S_1/S_0 crossing, all trajectories were restarted at the ground state with the same velocity and ran until a maximum time of 1000 fs.

The absorption spectrum and the initial conditions for dynamics were computed with the nuclear ensemble approximation,[42] sampling a quantum harmonic oscillator Wigner distribution with 500 points. The same number of excited states computed in the relaxed potential energy curves (24) was considered here. Dynamics simulations were started in two different spectral windows, 8.5±0.25 for a comparison with experimental data available, and 10.0±0.25 eV with the goal of analyzing the influence of higher Rydberg excited states in the photodissociation mechanism (the ionization energy of HCFC-132b obtained by photoelectron spectroscopy is 11.8 eV[43]). 100 points were stochastically sampled from each window according to their excitation probabilities. The distribution of the number of trajectories in each initial state is shown in Table 1. For dynamics simulations, the initial population in the low-energy window was distributed among the $n_{Cl(4)}$-σ*, $n_{Cl(3)}$-4p_z, and $n_{Cl(3)}$-4s excited states, while in the high-energy window the initial population was composed of the $n_{Cl(4)}$-4s, $n_{Cl(3)}$-4p_x, $n_{Cl(3)}$-4p_y, and $n_{Cl(3)}$-σ* excited states.

Table 1. Number of trajectories starting in each excited state in the two spectral windows considered in the present manuscript.

Window ΔE (eV)	Initial State									Total
8.25-8.75		S_6	S_7	S_8	S_9	S_{10}	S_{11}			
		12	28	31	19	6	4			100
9.75-10.25	S_{16}	S_{17}	S_{18}	S_{19}	S_{20}	S_{21}	S_{22}	S_{23}	S_{24}	
	5	11	13	13	14	10	13	11	10	100

Results and Discussion

Vertical Excitations and Excited-State Properties

Vertical excitation energies, oscillator strengths, and main configuration weights for each state, obtained from all levels of theory considered here, are given in Table 2 and S4 at

the supplementar material. Experimental photoabsorption data for HCFC-132b are available only for the band origin.[44] From now on, we will refer to each state in terms of the main configuration contributing to it, even when other configurations also have non-negligible weights.

The results show that the lowest vertical excitation corresponds to the $n_{yCl(3)}$-$\sigma^*_{C(1)Cl(3)}$ state, which is closely followed by the $n_{xCl(3)}$-$\sigma^*_{C(1)Cl(3)}$ state and then by the $n_{yCl(3)}$-$4p_z$ and $n_{yCl(4)}$-$4p_z$ Rydberg states (see Table 2). The two almost degenerate $n_{Cl(4)}$-$\sigma^*_{C(1)Cl(3)}$ states are assigned at ~ 8.2 eV, followed by the $n_{yCl(4)}$-$\sigma^*_{C(2)Cl(4)}$ state. In the range between 9.2 and 10.44 eV, a reasonably high number of n-Rydberg excited states are obtained. Interestingly, interspersed among these Rydberg states one has the $n_{xCl(4)}$-$\sigma^*_{C(2)Cl(4)}$ and $n_{yCl(3)}$-$\sigma^*_{C(2)Cl(4)}$ valence states at 9.41 and 10.27 eV, respectively.

Comparison between CASPT2, EOM-CCSD(T), and TD-DFT values of excitation energies are given in Figure 2. It reveals a good agreement between CASPT2 and the other two computational levels, with root-mean-square deviations (RMSD) of 0.15, 0.21, 0.32, and 0.37 eV for EOM-CCSD(T), TD-ωB97XD, TD-CAM-B3LYP and TD-M06-2X, respectively.

Excitation energies obtained with EOM-CCSD(T) are in very good agreement with CASPT2 and perform better than TD-DFT results. The nature of valence and Rydberg excited states are well described, a fact that highlights the reliability of CASPT2 results. In the EOM-CCSD(T) calculation, Rydberg states present a slightly higher mixture, but it did not represent a problem for the excited states characterization. On the other hand, with respect to TD-DFT results, TD-ωB97XD show better agreement with the corresponding CASPT2 results, especially for valence states. For instance, the excitation energies of the $n_{xCl(4)}$-$\sigma^*_{C(1)Cl(3)}$ and $n_{yCl(4)}$-$\sigma^*_{C(2)Cl(4)}$ states differ by only 0.03 and 0.09 eV, respectively, from those obtained at the CASPT2 level. The largest differences between the results obtained at these two levels are observed for higher Rydberg states, with the largest deviation (0.44 eV) for the $n_{yCl(3)}$-$4p_z$ state. For the remaining ones, the differences are lower than 0.35 eV. TD-CAM-B3LYP and TD-M06-2X results in general follow the same trend as TD-ωB97XD. However, excitation energies are higher, with few exceptions, for the $n_{yCl(4)}$-$4p_z$ and $n_{yCl(4)}$-$\sigma^*_{C(1)Cl(3)}$ states (see Table 2 and Figure 2).

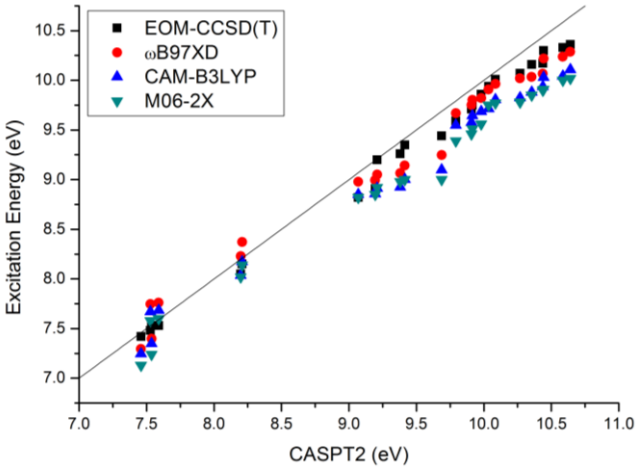

Figure 2. Correlation of CASPT2, TD-DFT, and EOM-CCSD(T) vertical excitation energies.

The valence states are characterized by large weights of the main configuration. Rydberg states, on their turn, show reasonably high configurational mixture (above 25%) between configurations of different Rydberg states, which can be explained by the small energy gap between them and the quasi-degeneracy in some cases. In spite of that mixing, the nature of the Rydberg states could be well characterized by the methods employed here.

Table 2. Vertical-excitation energies (eV), oscillator strengths, and configuration weights obtained for CF_2ClCH_2Cl molecule at the CASPT2, EOM-CCSD(T), and TD-ωB97XD levels with the aug-cc-pVDZ (C, F, H)/d-aug-cc-pVDZ (Cl) basis set.

States	MS-CASPT2			EOM-CCSD(T)			TD-ωB97XD		
	ΔE	Weights	f x 10^2	ΔE	Weights	f x 10^2	ΔE	Weights	f x 10^2
Gs	0.00	0.96	-	0.00	-	-	0.00	-	-
$n_{yCl(3)}$-$\sigma^*_{CCl(3)}$	7.46	0.61	0.10	7.42	0.68	0.13	7.296	0.58	0.19

$n_{xCl(3)}$-$\sigma^*_{CCl(3)}$	7.54	0.66	0.60	7.53	0.68	0.39	7.397	0.59	1.73
$n_{yCl(3)}$-$4p_z$	7.53	0.56	1.00	7.48	0.54	1.19	7.747	0.58	0.03
$n_{yCl(4)}$-$4p_z$	7.59	0.48	0.20	7.53	0.61	0.15	7.76	0.56	0.74
$n_{xCl(4)}$-$\sigma^*_{CCl(3)}$	8.20	0.68	2.20	8.05	0.56	1.49	8.23	0.63	1.32
$n_{yCl(4)}$-$\sigma^*_{CCl(3)}$	8.21	0.66	2.50	8.15	0.64	2.69	8.371	0.63	1.88
$n_{yCl(4)}$-$\sigma^*_{CCl(4)}$	9.07	0.64	9.50	8.82	0.66	8.30	8.979	0.46	0.96
$n_{xCl(3)}$-$4p_z$	9.20	0.56	2.90	8.91	0.66	2.20	8.994	0.50	8.44
$n_{yCl(3)}$-4s	9.21	0.66	6.30	9.20	0.68	5.20	9.052	0.48	4.51
$n_{xCl(3)}$-4s	9.38	0.71	1.10	9.26	0.68	1.97	9.066	0.48	3.28
$n_{xCl(4)}$-$\sigma^*_{CCl(4)}$	9.41	0.6	0.20	9.35	0.70	0.72	9.142	0.64	4.97
$n_{yCl(3)}$-$4p_z$	9.69	0.73	1.00	9.44	0.70	0.27	9.248	0.65	0.38
$n_{xCl(3)}$-$4p_y$	9.79	0.54	41.70	9.59	0.67	0.03	9.669	0.48	0.32
$n_{yCl(4)}$-$4p_x$	9.91	0.59	0.30	9.71	0.64	0.75	9.751	0.41	1.08
$n_{xCl(4)}$-$4p_x$	9.92	0.71	3.30	9.75	0.67	0.65	9.802	0.45	3.29
$n_{yCl(3)}$-$4p_x$	9.98	0.59	1.30	9.86	0.64	1.40	9.821	0.35	13.66
$n_{yCl(4)}$-4s	10.04	0.88	0.70	9.94	0.68	0.65	9.908	0.34	0.17
$n_{xCl(4)}$-$4p_y$	10.09	0.5	1.50	10.01	0.65	0.59	9.964	0.38	7.56
$n_{yCl(3)}$-$\sigma^*_{CCl(4)}$	10.27	0.73	0.10	10.07	0.56	0.23	10.021	0.62	12.91
$n_{yCl(4)}$-$4p_y$	10.35	0.8	1.50	10.16	0.64	0.78	10.034	0.28	0.00
$n_{xCl(4)}$-4s	10.44	0.69	1.10	10.17	0.70	0.01	10.067	0.51	0.52
$n_{yCl(3)}$-$4p_y$	10.44	0.77	0.10	10.30	0.69	0.42	10.218	0.49	2.00
$n_{xCl(3)}$-$\sigma^*_{CCl(4)}$	10.59	0.69	1.80	10.33	0.67	0.19	10.237	0.53	2.51
$n_{xCl(3)}$-$4p_x$	10.64	0.72	0.00	10.36	0.68	0.64	10.288	0.59	0.01

As can be seen from Table 2, the oscillator strength (*f*) value computed at the CASPT2 level is the highest for the $n_{xCl(3)}$-$4p_y$ state, followed by those of $n_{yCl(4)}$- $\sigma^*_{CCl(4)}$ and $n_{yCl(3)}$-4s states. The next highest *f* value, that of $n_{xCl(4)}$-$4p_x$ state, is about half of that of $n_{yCl(3)}$-4s. The lowest *f* value was obtained for the $n_{xCl(3)}$-$4p_x$ transition. Notice that this latter transition represents a virtually forbidden transition.

For most of the valence states there is reasonably good agreement of the *f* values computed at the CASPT2, EOM-CCSD(T), and TD-ωB97XD levels. However, while for the $n_{xCl(3)}$-$\sigma^*_{CCl(3)}$ and $n_{xCl(4)}$-$\sigma^*_{CCl(4)}$ states they are considerably overestimated at EOM-CCSD(T) and TD-ωB97XD levels, for the $n_{yCl(3)}$-$\sigma^*_{CCl(4)}$ state the *f* value is considerably underestimated (see Table 2). Notice that the former pair of states involves a transition in the *x* direction, which is localized in the same region of the molecule (intra-region); while the latter involves a transition in the *y* direction, which is from one region to another (inter-region). The TD-ωB97XD *f* values corresponding to such inter-region transitions involving the Cl(4) lone pairs show good agreement with those at the CASPT2 level for

both (*x* and *y*) polarizations. For the intra-region transitions involving this same atom, only that one polarized in the *y* direction is well described at the TD-ωB97XD level (see Table 2). The same holds for this latter type of transition involving Cl(3), but for the former type of transition involving this same atom, a good agreement is achieved only for the *x*-polarized transition.

At both CASPT2 and TDDFT levels, the largest *f* value was obtained for an n-4p Rydberg state. Although they differ (that is, at the former level, it is the $n_{xCl(3)}$-$4p_y$ state, while at the latter it is the $n_{yCl(3)}$-$4p_x$), the energy difference between these two states is only 0.19 eV at the CASPT2 level. Besides, the transitions that they represent have the same polarization and are localized in the same Cl atom. The CASPT2 results for the *x* polarized n-4s transitions involving the Cl(3) and Cl(4) atoms are practically the same, while at the TD-ωB97XD level, they are overestimated and underestimated, respectively, by about the same extent. On the other hand, the corresponding *y* polarized transition involving the Cl(3) atom ($n_{yCl(3)}$-4s) is well described, while that one involving the Cl(4) atom is overestimated (see Table 2). Most of the n-4p transitions with change of polarization involving Cl(3) are significantly underestimated at the TD-ωB97XD level. The only exception is the $n_{yCl(3)}$-$4p_x$ transition, whose *f* value is considerably overestimated at this level. However, as aforementioned, this transition is very similar to the $n_{xCl(3)}$-$4p_y$ transition at the CASPT2 level (see Table 2). The best agreement between CASPT2 and TD-ωB97XD results concerning n-4p Rydberg transitions is achieved for the $n_{xCl(3)}$-$4p_x$, $n_{yCl(4)}$-$4p_y$, $n_{yCl(3)}$-$4p_z$, $n_{yCl(4)}$-$4p_z$, $n_{xCl(4)}$-$4p_y$, and $n_{yCl(4)}$-$4p_x$ transitions, in the descending order of agreement. Although the differences are not negligible, the *f* values obtained at these two levels have the same order of magnitude. The largest discrepancies between CASPT2 and TD-ωB97XD results were obtained for the $n_{xCl(3)}$-$4p_z$ and $n_{xCl(4)}$-$4p_x$ states. In these two cases, the *f* values obtained at the latter level are highly underestimated. In summary, the performance of ωB97XD functional is acceptable. However, the general performance of the CAM-B3LYP functional is poorer and thus it will not be further discussed.

Concerning the performance of TD-ωB97XD for describing dissociation processes, we have computed the potential energy profiles along the C-Cl bonds at TD-ωB97XD and CASPT2 levels. They can be seen in Figure S5 of the Supporting Information. Compared to CASPT2, TD-ωB97XD performs reasonably well to describe the crossings between

excited states in the pre-dissociated region and the first asymptotic level (ground and first excited state). Higher asymptotic levels for dissociation of other states are poorly described though. As discussed later, the population distribution of HCFC-132b is determined by its early dynamics, during a quick nonadiabatic relaxation, followed by dissociation occurring along the lowest asymptotic levels. These are regions where TD-ωB97XD still holds a good comparison with CASPT2, meaning that the method may be cautiously employed for dynamics simulations of HCFC-132b.

UV-Photoabsortion Spectrum and Initial Conditions

The result of HCFC-132b UV-photoabsortion spectrum is shown in Figure 3. It was simulated using the nuclear-ensemble approach, which provides absolute intensities and band widths, but does not include vibrational resolution.[45] As TD-ωB97XD results show good agreement with CASPT2, for both vertical excitation energies and potential energy curves, it has been chosen for spectrum and nonadiabatics dynamics simulations.

In the region up to 10.5 eV the absorption spectrum shows four bands, two with high intensity with peaks at 9.0 and 9.8 eV, a third one with lower intensity at 8.3 eV, and another very weak at 7.6 eV. The most intense band at 9.8 eV has clear shoulders at 9.9 and 9.7 eV. The comparison of these spectral features with the vertical transitions allows the direct assignment of them.

The 7.6 and 8.3 eV bands correspond to n-σ* excitation. The first is associated with chlorine atom from CF_2Cl group, an intra-region $n_{Cl(3)}$-$\sigma^*_{CCl(3)}$ excitation, and the second one corresponds to an inter-region transition from the Cl(4) lone pair, a $n_{Cl(4)}$-$\sigma^*_{CCl(3)}$ excitation (see Table 2). The 9.0-eV band is mainly composed of the $n_{Cl(3)}$-4s low-lying Rydberg excitation, while the 9.8-eV band is due to the $n_{Cl(3)}$-$4p_x$ state. The 9.7 and 9.9 eV shoulders correspond respectively to the $n_{Cl(3)}$-$4p_y$ and $n_{Cl(4)}$-$4p_y$ states.

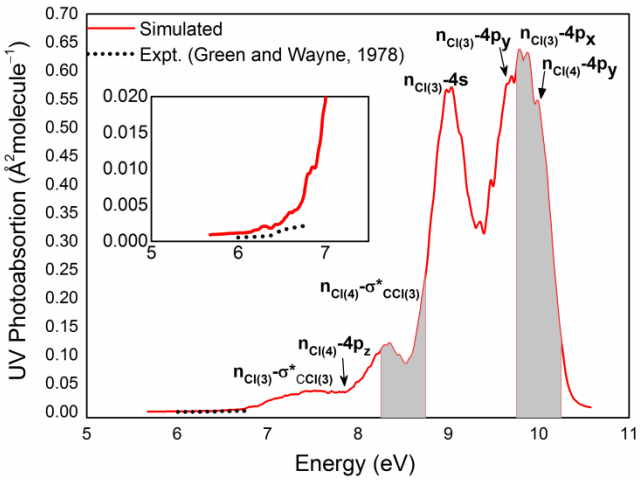

Figure 3. Absorption cross sections of HCFC-132b calculated at the TD-ωB97XD/aug-cc-pVDZ (C, F and H)/d-aug-cc-pVDZ (Cl) level. The dotted line is the experimental result from Ref.[44]. The shaded areas indicate the regions sampled for initial conditions for dynamics simulations. The inset shows the band-origin region in detail.

Experimentally, photochemical information is available at 147 nm wavelength (8.43 eV).[22] This excitation region is located near the center of the 8.3-eV band, which is due to $n_{Cl(4)}$-σ*$_{CCl(3)}$ excitations and associated to carbon-halogen bond fission.[46] Nevertheless, this excitation region is also at the edge of the 9.0-eV band, implying that it also has strong contributions from n_{Cl}-4s excitations, which are directly associated with the elimination of molecular products.[47] Such overlap between n_{Cl}-σ*$_{CCl}$ and n_{Cl}-4s states is common in the photoabsorption spectra of a number of CFCs[48] and HCFCs.[49] It suggests the existence of crossings between these excited states. This spectral characteristic helps to explain the preference of the molecule for multifragmentation or single bond breakage reaction paths in certain excitation windows. However, for HCFCs with more than one chlorine atom, where the reaction paths are more diverse, multifragmentation can take place instead of single carbon-halogen dissociation.

Photoproducts and Excited-State Lifetimes

Dynamics simulations were performed in two different spectral windows, with initial excitation energies centered at 8.5 and 10.0 eV. The dynamics starting in each of these windows leads to different distributions of a number of photochemical products. The fractions of these products are reported in Table 3. Theoretical error bars were computed

for 90% confidence interval.

Table 3. Percentages of each product obtained in the simulations and in the experiments.

	Experimental (%)*	Theoretical (%)	
	8.43 eV	window 8.5 eV	window 10.0 eV
2Cl	41	42±8	9±5
HCl	4.8	19±7	33±8
CFB[a] / Cl	41.3	34±8	21±7
FCl	-	-	2±2
HF	-	5±4	23±7
F	-	-	3±3
H	-	-	3±3
CC	-	-	6±4

*Excitation at 147 nm, 2.5 Torr, without added gases[22]; [a]CFB: chlorofluorbutanes; the theoretical value for Cl release comes from an indirect measurement of CFB formation (see text for details).

In the 8.5-eV excitation window, two main reaction channels were observed: the simultaneous dissociation of both chlorine atoms (42%) and single chlorine-carbon bond breakage (34%). Dissociation of HCl appears as the third pathway in terms of photoproducts (19%). A minor reaction channel, with 5% contribution, was also detected. It corresponds to a double fragmentation of Cl and F atoms, with subsequent recombination and HF formation in the hot ground state.

In the case of the 10.0-eV excitation window, an even larger diversity of photochemical reaction paths is observed. Cl, HF, and HCl dissociations are the main photoproducts, corresponding to 21%, 23%, and 33%, respectively. One also detects other minor channels: dissociation of two Cl atoms (9%), CC bond breakage (6%), dissociation of F or H atoms (3% each), and FCl dissociation (2%).

Experimentally,[22] the photodecomposition of HCFC-132b after 147 nm (8.43 eV) shows two main photochemical products: the simultaneous dissociation of two chlorine atoms (41%) and the formation of chlorofluorobutanes (41.3%); moreover, a small quantity of HCl formation is also observed (4.8%).[22] The comparison between these experimental results and theoretical simulations at the 8.5-eV excitation window shows good agreement (see Table 3). In particular, taking into account the error bars of the simulations, the two main channels — release of Cl and 2Cl — closely agree with the

experimental results.

The double chlorine release takes place preferentially when the system is still in the excited states. The two chlorine atoms can be eliminated simultaneously or sequentially. Experimentally, these pathways could not be discriminated and they contribute to the total amount of Cl atoms generated. However, in our simulations we were able to differentiate these two photo-decay processes.

The second main photochemical reaction channel corresponds to single chlorine-carbon bond fission (34%). This amount of Cl atoms generated can be interpreted as a source of formation of multi-fragmented products in the hot ground state. Chlorine atoms can also be associated to the formation of chlorinated-fluoro-butanes (CFB) products of bimolecular recombination of monochlorinated radicals (as for instance, ClF_2CCH_2 or F_2CCClH_2). Thus, if such reactions are the main route to CFB formation, the presence of atomic chlorine in the system can be considered the main pathway to the formation of CFB.[22] For this reason, although our simulations are limited to a single molecule and thus cannot include the bimolecular CFB formation, we have taken the Cl release as an indirect measure of CFB formation.

According to the experiments, the HCl channel contributes with only 4.8% of the photoproducts. However, our simulations have predicted a relatively larger amount of HCl formation, 19%. As single chlorine is mainly generated in the excited state, some of these atoms return to the ground in a hot state, promoting recombination reactions with H atoms, which explains the larger amount of this product observed theoretically.

The amount of correlation between the character of the initially photoexcited state and the formed product depends on the excitation window. At the 8.5-eV window, the direct population of low energy n-σ* states leads mainly to single C-Cl bond breakage; on the other hand, population of n-4s and n-4p Rydberg states leads to multi-fragmented products, highlighting the importance of low-lying Rydberg states in the photochemistry of this group of compounds. At the 10-eV window, it is not observed a direct influence of the initial state on the resulting products. However, the population of higher states at this excitation window clearly leads to new reaction pathways associated with multi-fragmented products.

The excited-state lifetimes were calculated by fitting the excited state population

(summed over all excited states) by an exponential decay function given in Eq.(1)[41] (Figure S2):

$$f(t) = f_0 \exp\left(-\frac{(t-\tau_L)}{\tau_D}\right), \quad (1)$$

where τ_L is the latency time to initiate the nonadiabatic process, τ_D is the deactivation time, and f_0 is the fraction of population that does not decay to the ground state through ultrafast processes. This latter parameter was taken as zero during the fitting process. The excited-state lifetime (τ) is given by the sum of τ_L and τ_D. Table 4 shows the excited-state lifetimes obtained in both excitation windows. In both cases the deactivation process is ultrafast, taking less than 200 fs. Deactivation tends to be faster in the 8.5-eV window, as expected, as fewer states should be crossed until the system returns to the ground state.

Table 4. Excited-state lifetimes τ (fs) obtained by fitting the exponential decay function given in Eq. (1). Estimated errors are ±7 and ±9 fs for the 8.5 and 10 eV excitation windows, respectively.

Window ΔE (eV)	τ_L (fs)	τ_D (fs)	τ (fs)
8.5	32	74	106
10.0	65	126	191

Photochemical Reaction Paths

At the 8.5-eV excitation window

When HCFC-132b is excited at the 8.5 eV spectral window, the $n_{Cl(4)}$-$\sigma^*_{CCl(3)}$, n_{Cl}-$4p_Z$, and $n_{Cl(3)}$-4s states are populated. These excited states represent the route to atomic chlorine and chlorinated products.

Regarding single Cl formation, single carbon-halogen cleavage is already expected, as states involving C-Cl bonds for HCFC are present in the region of 8.0±0.5 eV, depending on the number of halo-substituents. The decay process for single Cl atom can be observed in the qualitative scheme shown in Figure 4. Starting the dynamics in the n-σ* or n-4s states, the system easily decays to n-$4p_z$ Rydberg states, which are essential to the products formation. Our simulations show that the system can follow two distinct pathways: in the first one, it remains in the n-4s state during a period of time long enough for a stabilization of 4p Rydberg orbital (about ~40 fs). As 4s and $4p_z$ orbitals are in the same symmetry plane, an interaction between them is favored. Consequently, there is an

inversion in which 4p orbital assumes LUMO position, promoting Cl formation in the n_{Cl}-$4p_z$ excited state, instead of in the valence states (right side - Figure 4).

In the second pathway leading to single Cl formation, the molecule quickly relaxes from the n_{Cl}-$4p_z$ state to low-lying n-σ* states. In this case, Cl formation takes place only after conversion to the ground state via internal conversion. Until the system populates n-4s excited states the process is similar to the previous one. Upon increase of the $R_{C\text{-}Cl}$ distance with subsequent bond breakage the chlorine fragment readily flies away from the rest of the molecule. Immediately after this step it decays to n-4p and readily decays thought an intersection to n-σ* (left side - Figure 4) and the dissociation process is finished after internal conversion to the ground state.

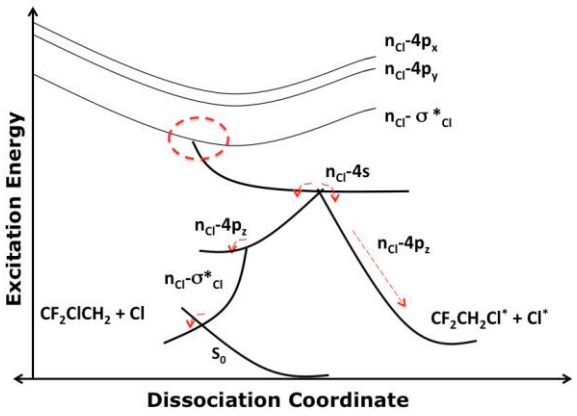

Figure 4. Schematic qualitative pathways to single Cl formation. The dashed circle indicates the absorption region.

The dissociation process leading to 2Cl can take place in two distinct ways as well. In the first and more frequent way, fast and almost simultaneous carbon-halogen bond breakage (still in the excited state) leads to dissociation of two Cl atoms. Alternatively, 2Cl products may result from initial dissociation of a single Cl atom, followed by migration of the other Cl to the opposite carbon, with the second dissociation occurring after internal conversion to the ground state. The activation of one or other pathway for 2Cl formation is related to the time that the molecule remains in the n-4s states. If from these states, it decays within approximately 30 fs to the n-σ* states characterized by intra-region orbitals interactions (that is, $n_{Cl(3)}$-$\sigma^*_{CCl(3)}$ or $n_{Cl(4)}$-$\sigma^*_{CCl(4)}$), both Cl fragments are quickly released, and after that a S_1/S_0 intersection is reached, which finishes the process (left side

of Figure 5). On the other hand, if the molecule remains longer at the n-4s states, there is enough time for an interaction between the n-σ* states composed of inter-region interactions. The migration of one fragment before its release promotes a crossing between these states ($n_{Cl(4)}$-$\sigma^*_{CCl(3)}$ or $n_{Cl(3)}$-$\sigma^*_{CCl(4)}$) and a subsequent decay via lower-lying $n_{Cl(3)}$-$\sigma^*_{CCl(3)}$ or $n_{Cl(4)}$-$\sigma^*_{CCl(4)}$ states (right side of Figure 5), followed by internal conversion to the ground state.

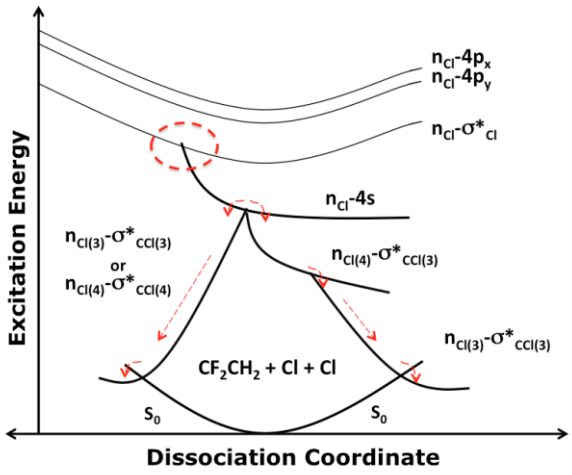

Figure 5. Qualitative scheme showing the two pathways for formation of 2Cl.

In the case of HCl formation, the photochemical process initiates as the single Cl formation aforementioned. Upon n-4s population, Cl release takes place, followed by decay mainly to n-4p$_z$ states. Conformational changes result in carbon-hydrogen bond breakage. Afterwards the system proceeds to a crossing with n_{Cl}-σ^*_{CH} excited states. Finally, the molecule quickly relaxes to the ground state via internal conversion, leading to HCl formation. This process is schematically shown in Figure 6 (right side). The left side of this figure also shows the key steps in the production of HF after 8.5eV excitation.

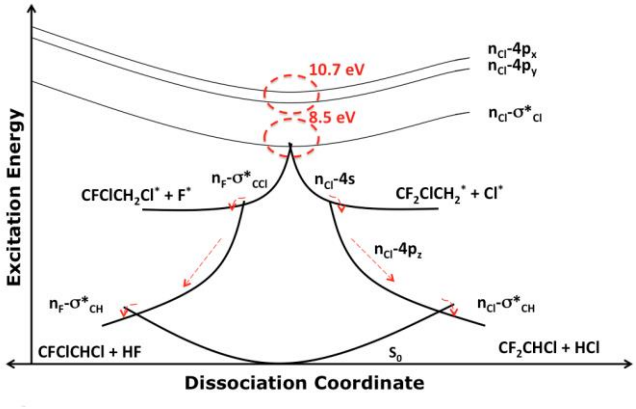

Figure 6. Qualitative scheme showing photo-processes leading to HCl and HF formation. Dashed circles indicate the absorption region in both energy windows.

At the 10.0-eV excitation window

The main states involved in the photochemistry of HCFC-132b upon excitation in the 10.0 eV window are the n_{Cl}-4p_x, n_{Cl}-4p_y, $n_{Cl(3)}$-σ*$_{CCl(4)}$ and $n_{Cl(4)}$-4s. Excitation of halothanes in higher energies may promote formation of long-living Rydberg states, leading the system to a different photo-decay process and consequently to a diversity of non-chlorinated products.

Photochemical production of HCl and C-Cl bond breakage are already observed in 8.5-eV excitation window previously analyzed. However, they do not represent the main reaction pathways. Instead, the excitation of HCFC-132b in a higher energy region promotes formation of significant amounts of HCl and C-Cl bond breakage, where these photoproducts sum to 54% of the total yield. As the system populates long-living high-energy states, it promotes the dissociation of different multi-fragmentation products. Another important characteristic is the production of a significant amount of HF in this second region. The appearance of long-living Rydberg states (in general, the system spends around 90 fs on high Rydberg states) leads the molecule to decay to pathways which yields non-chlorinated species and dissociate in products associated with C-F, C-H, and C-C bond breakage.

Regarding to 2Cl, Cl, and HCl formation processes, they occur in the same way as explained for the 8.5-eV window. The only difference here is that the system takes longer to reach states of lower energy. The chlorine fragments are mainly produced in the excited

state. However, H formation usually takes place when a S_1/S_0 intersection is reached. Then H and Cl fragments recombine to yield HCl molecule. The HF formation process is qualitatively depicted in Figure 6 (left side). It initiates in high-lying n-4p Rydberg states. If the molecule remains for a relatively long time in these states (about ~30 fs), conformational changes, such as a strong C-F bond stretching or FCCCl dihedral angles twist, can take place, which stabilizes the n_F orbital and lead the system to relax throught a n_F-σ^*_{CCl} state, in which F atom is released. Then, the system proceeds to an n_F-σ^*_{CH} state, finally resulting in the F+H multi-fragmentation. Already in the ground state, they recombine as a HF molecule.

The breakage of C-F, C-H, or C-C bonds represents 11% of the products. F atom generating pathway is shown in Figure 7 (left side). It happens when structural changes lead the system to excited states characterized by interaction between orbitals of Cl and F atoms. Specifically in the case of F generation, n_{Cl} orbitals interact with σ^*_{CF} and the system quickly decays to the n_F- σ^*_{CF} excited state. The relaxation along S_1 and increase of CF distance until ~ 3.1 Å lead to intersection with S_0 (the initial CF equilibrium distance is ~1.52 Å), where conversion to the ground state takes place.

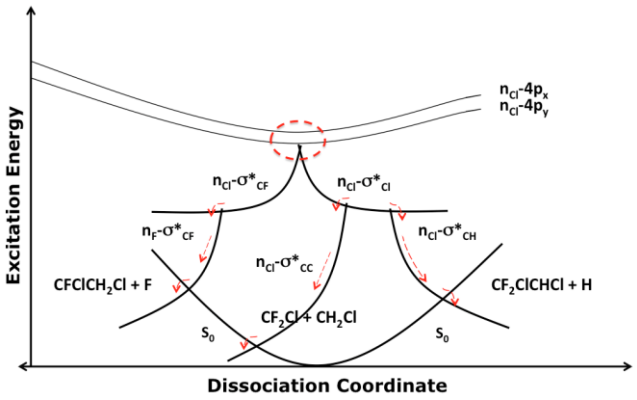

Figure 7. Qualitative Scheme representing single CF, CH and CC bonds fission.

The H release is depicted in Figure 7, right. The reaction starts with the decay from n-4p to a higher n_{Cl}-σ_{Cl}* state, which has a CH equilibrium distance around 1.2 Å. A subsequent crossing with σ_{Cl}-σ^*_{CH} state promotes CH bond breaking with relaxation along S_1 followed by a return to S_0 via internal conversion.

The third pathway here discussed is the CC bond fission. The photochemical process

begins with a relaxation from an initial n-4p excited state to an n_{Cl}-σ_{Cl}* state, followed by a fast decay to an n_{Cl}-σ_{CC}* state, in which the CC bond breakage takes place (Figure 7, middle). Upon the decay process and separation of CF_2Cl and CH_2Cl fragments it finds an intersection with the ground state.

Conclusions

The UV-photoexcitation of HCFC-132b (CF_2ClCH_2Cl), a pollutant related to atmospheric ozone deflection and global warming, was investigated at CASPT2, CCSD(T), and TDDFT levels through calculations of absorption spectrum, potential energy curves, and nonadiabatic dynamics simulations.

Energy ordering and excited-state characters calculated with TD-ωB97XD are in good agreement with CASPT2 and CCSD(T) results. Internal conversion to the ground state takes place within 106 and 191 fs at 8.5 and 10 eV excitation windows, respectively. The molecule decays through a large variety of reaction mechanisms and the excitation region plays an important role on the products yield. For the 8.5-eV region, single Cl, 2Cl, and HCl are the main photoproducts. HF appears as a minor product. On the other hand, excitation in the 10.0-eV region leads to a significant decrease in the yields of 2Cl and Cl, and to a significant increase in the amount of HCl and HF products, as well as to the appearance of other products associated with FCl and F, H, and CC bond breakage. A complete assignment of the states involved in each of these mechanisms is provided.

For the first time, photochemical pathways of HCFC-132b have been described and reaction paths characterized. Taking into account the statistical uncertainties the results of the simulated fragmentation are consistent with experimental available data, where 2Cl, HCl, and chlorofluorbutanes (CFB) are mainly produced. The elimination of 2Cl should take place most likely in the excited state, as well as C-Cl bond breakage for subsequent recombination and CFB formation in the ground state. However, HCl and HF fragmentation should have a significant contribution from ground-state recombination. Finally, FCl fission should occur exclusively in the excited state, followed by recombination in the ground state.

Acknowledgments

The authors acknowledge Brazilian agencies CAPES and CNPq (Project 232180/2013-0), and the German agency DAAD for the financial support. MB thanks the support of the A*MIDEX grant (n° ANR-11-IDEX-0001-02) funded by the French Government « Investissements d'Avenir » program.

References

1. D. L. Downie. "The Vienna Convention, Montreal Protocol and Global Policy to Protect Stratospheric Ozone"; Taylor & Francis: Oxford, **2012**.

2. M. J. Molina, F. S. Rowland. *Nature* **1974**, 249, 810-812.

3. D. Newnham, J. Ballard. *J. Quant. Spectrosc. Radiat. Transfer* **1995**, 53, 471-479.

4. G. Di Lonardo, G. Masciarelli. *J. Quant. Spectrosc. Radiat.Transfer.* **2000**, 66, 129-142.

5. United Nations Framework Convention on Climate Change. Kyoto, **1997**.

6. S. O. Andersen, K. M. Sarma. Protecting the Ozone Layer: the United Nations History; Earthscan Press: London, **2002**.

7. S. O. Andersen, K. M. Sarma, K. N. Taddonio. Technology Transfer for the Ozone Layer: Lessons for Climate Change; Earthscan Press: London, **2007**.

8. D. L. Downie. "Stratospheric Ozone Depletion."; Routledge: New York, **2013**.

9. COWIconsult Consulting Engineers and Planners AS. Reduction of CFC-Consumption - Anex Report; Nordic Council of Ministers: Copenhagen, **1989**.

10. O. Hedenstrom. Conditions for reducing CFC emission in connection with manufacture of expanded foam and reduction of CFC-release by dry cleaning, degreasing and drying; Prikon AB for Statens Naturvardsvek: Swedish, **1987**.

11. U.S. Department of State. Chlorofluorocarbon chemical substitutes; EPA:

Washington, DC, USA, **1986**.

12. M. W. Anders. *Environ. Health Persp.* **1991**, 96, 185-191.

13. D. E. Dodd, W. T. Brashear, A. Vinegar. *Toxicol. Lett.*, 68, 37-47.

14. J. W. Harris, M. W. Anders. *Chem. Res. Toxicol.* **1991**, 4, 180-186.

15. M. L. Deviney Jr., W. A. Felsing. *J. Am. Chem. Soc.* **1957**, 79, 4915-4917.

16. J. B. Cross, J. Lielmezs. *J. Chem. Eng. Data.* **1967**, 12, 75-77.

17. P. H. Smith, W. P. Kilroy, S. D. James. *J. Chem. Eng. Data.* **1984**, 29, 284-286.

18. T. Yano, K. H. Jung, E. Tschuikow-Roux. *J. Phys. Chem.* **1980**, 84, 2146-2151.

19. T. Yano, E. Tschuikow-Roux. *J. Chem. Phys.* **1980**, 72, 3401-3409.

20. T. Yano, E. Tschuikow-Roux. *J. Phys. Chem.* **1980**, 84, 3372-3377.

21. T. Yano, S. Ozaki, H. Ogura, E. Tschuikow-Roux. *J. Phys. Chem.* **1985**, 89, 1108-1116.

22. T. Yano, E. Tschuikow-Roux. *J. Phys. Chem.* **1979**, 83, 2572-2578.

23. G. P. Rodrigues, J. R. Lucena Jr., E. Ventura, S. A. do Monte, I. Reva, R. Fausto. *J. Chem. Phys* **2013**, 139, 10.

24. G. P. Rodrigues, E. Ventura, S. A. Do Monte, M. Barbatti. *J. Phys. Chem. A* **2014**, 118, 12041-12049.

25. C. Moller, M. S. Plesset. *Phys. Rev.* **1934**, 46, 618-622.

26. R. A. Kendall, T. H. Dunning Jr., R. J. Harrison. *J. Chem. Phys.* **1992**, 96, 6796-6807.

27. M. J. Frisch, G. W. Trucks, H. B. Schlegel, G. E. Scuseria, M. A. Robb, J. R. Cheeseman, G. Scalmani, V. Barone, B. Mennucci, G. A. Petersson, et al. **2013**.

28. T. H. Dunning Jr. *J. Chem. Phys.* **1989**, 90, 1007-1023.

29. D. E. Woon, T. H. Dunning Jr. *J. Chem. Phys.* **1994**, 100, 2975-2999.

30. F. Aquilante, L. De Vico, N. Ferre, G. Ghigo, P. A. Malmqvist, P. Neogrady, T.

B. Pedersen, M. Pitonak, M. Reiher, B. O. Roos, L. Serrano-Andrés, M. Urban, V. Veryazov, R. Lindh. *J. Comput. Chem.* **2010**, 31, 224-247.

31. M. S. Gordon, M. W. Schmidt. In Theory and Applications of Computational Chemistry: the first forty years; C.E.Dykstra, G. F., K.S.Kim, G.E.Scuseria Ed.; Elsevier: Amsterdam, **2005**, p 1167-1189.

32. T. Yanai, D. P. Tew, N. C. Handy. *Chem. Phys. Lett.* **2004**, 393, 51-57.

33. J. D. Chai, M. Head-Gordon. *Phys. Chem. Chem. Phys.* **2008**, 10, 6615-6620.

34. Y. Zhao, D. G. Truhlar. *Theor. Chem. Acc.* **2008**, 120, 215-241.

35. J. C. Tully. *J. Chem. Phys.* **1990**, 93, 1061-1071.

36. M. Barbatti. *WIREs: Comp. Mol. Sci.* **2011**, 1, 620-633.

37. G. Granucci, M. Persico. *J. Chem. Phys.* **2007**, 126, 134114.

38. M. Barbatti, M. Ruckenbauer, F. Plasser, J. Pittner, G. Granucci, M. Persico, H. Lischka. *WIREs: Comput. Mol. Sci.* **2014**, 4, 26-33.

39. M. Barbatti, G. Granucci, M. Ruckenbauer, F. Plasser, R. Crespo-Otero, J. Pittner, M. Persico, H. Lischka. **2013**.

40. M. E. Casida, M. Huix-Rotllant. *Annu. Rev. Phys. Chem.* **2012**, 63, 287-323.

41. F. Plasser, R. Crespo-Otero, M. Pederzoli, J. Pittner, H. Lischka, M. Barbatti. *J. Chem. Theory Comput.* **2014**, 10, 1395-1405.

42. R. Crespo-Otero, M. Barbatti. *Theor. Chem. Acc.* **2012**, 131, 1237.

43. J.-M. Dumas, P. Dupuis, G. Pfister-Guillouzo, C. Sandorfy. *Can. J. Spectrosc.* **1981**, 26, 102.

44. R. G. Green, R. P. Wayne. *J. Photochem.* **1976-1977**, 6, 375-377.

45. R. Crespo-Otero, M. Barbatti. *Theor. Chem. Acc.* **2012**, 131, 1237.

46. T. Fujimoto, M. H. Wijnen. *J. Chem. Phys.* **1972**, 56, 4032-4035.

47. C. Hubrich, F. Stuhl. *J. Photochem.* **1980**, 12, 93-107.

48. S. Eden, P. Limão-Vieira, S. V. Hoffmann, N. J. Mason. *Chem. Phys.*, 323, 313-332.

49. J. Doucet, P. Sauvageau, C. Sandorfy. *J. Chem. Phys.* **1973**, 58, 3708-3716.